Applied Sciences, Computing and Energy, 2024, 1(1), 356- 369

Integrated Analysis of Mechanical Thinning and Thermal Subsidence in Engineering Materials and Systems

Oyeniyi Richard Ajao*, Kazeem Bamidele Ajanaku, Oladipupo Opeyemi Solaja, and Arunprasath Muthuramalingam[4].

Received: 14 August 2024/Accepted: 23 December 2024/Published:31 December 2024

Abstract: *Structural degradation of engineering materials via the intertwined processes of mechanical thinning and thermal subsidence has become a chronic and, in reality, often underestimated problem over a broad spectrum of industrial applications, including aeronautical structures and subsea pipelines, onshore and offshore infrastructure and energy conversion systems. Mechanical thinning: the progressive loss of cross-sectional material due to plastic deformation, abrasion, or controlled manufacturing processes, which changes load-bearing capacity and stress distribution in a manner that is not always reflected in conventional safety margins. Superimposed on thermal subsidence, which in this context is the thermally induced vertical movement and volumetric contraction of material systems under constant or a varying load in terms of temperature, the damage accretion may proceed with rates generally much larger than either of these mechanisms would yield in the absence of the other. In this paper, an analytical and numerical framework has been integrated in the characterization of the interaction between these two degradation echanisms in metallic alloys and composite structures of engineering interest. Based on finite element simulations that have been validated using experimental data obtained through tensile coupons and profilometric thinning measurements, thermocouple-measured subsidence experiments, we can determine quantitative relations between thinning severity indices, magnitude of thermal gradients, and the development of concurrent failure modes such local buckling, creep-assisted cracking, and interfacial delamination. A parametric study of carbon steel (ASTM A36), aluminium alloy (6061-T6) and a unidirectional carbon-fibre reinforced polymer (CFRP) laminate indicates that thermal cycling between, at least, -40°C and 250°C expedites the subsidence-induced displacement by a factor of up to 34 in pre-thinned specimens as compared to nominal geometry controls. The findings carry direct implications for inspection scheduling, remaining useful life (RUL) estimation, and structural health monitoring protocols, and they challenge the adequacy of standards that treat thinning and thermal effects as independently additive degradation factors.*

Keywords: *Mechanical thinning; thermal subsidence; coupled degradation; finite element analysis; remaining useful life; creep; composite laminates*

Oyeniyi Richard Ajao
Yale School of Management, New Haven, Connecticut, USA.
Email: oyeniyiajao10@gmail.com

Kazeem Bamidele Ajanaku
Department of Mechanical Engineering, College of Engineering and Technology, Ladoke Akintola University of Science and Technology, Ogbomosho, Nigeria.
Email: bamideleajanaku1@gmail.com

Oladipupo Opeyemi Solaja
Department of Business Administration, University Canada West, Vancouver, British Columbia, Canada.
Email: solajaoladipupo1@gmail.com

Arunprasath Muthuramalingam
Mechanical Engineering Department, Faculty of Engineering and Technology, Birla Institute of Technology and Science, Vidya Vihar, Pilani, Rajasthan, India.
Email: er.arunprasath@yahoo.com

1.0 Introduction

Engineering structures rarely fail through a single, cleanly isolated mechanism. The more instructive and more dangerous failure histories invariably involve the convergence of two or more degradation pathways that, operating simultaneously, create synergistic damage accumulation that neither classical design standards nor routine inspection protocols are fully equipped to anticipate. The interaction between mechanical thinning and thermal subsidence represents one such convergence, yet this coupled interaction remains insufficiently examined in the open literature, given how commonly it occurs in practice. Offshore oil and gas platforms, heat recovery steam generators, aircraft fuselage panels, and reinforced-concrete bridge decks each provide plausible scenarios in which a structurally reduced cross-section is simultaneously subject to a sustained or cycling thermal load and yet, the majority of fitness-for-service (FFS) assessments still treat these effects as independent additive contributions to a net safety margin (Ainsworth 2006; American Petroleum Institute / ASME 2021).

Mechanical thinning is the progressive loss of effective material thickness or cross-sectional area caused by plastic deformation, abrasion, corrosion, or manufacturing processes. This includes controlled industrial operations such as cold rolling, deep drawing, and machining, as well as unintended processes such as uniform corrosion, erosion-corrosion in multiphase flow environments, cavitation damage, and abrasive wear. The consequences of thinning are intuitively obvious at some level: a thinner section carries higher nominal stress for the same applied load, and local thinning introduces geometric discontinuities that serve as stress concentrators. What is less obvious and where the engineering literature has made more variable progress is the manner in which thinning modifies the thermal response of a component, particularly when the temperature distribution across that component is itself non-uniform (Zhu & Chao 2002; Lee& Chan 2019). “Consequently, thinning not only alters mechanical resistance but also modifies thermal transport characteristics, thereby creating conditions for coupled thermo-mechanical degradation.

Thermal subsidence, as employed in this paper, denotes the thermally driven downward displacement and associated volumetric change that a material or structural element undergoes when heated or cooled through a significant temperature range. This is very familiar in geomechanics, where cooling of the lithosphere after the onset of volcanism or rifting leads to observable subsidence of the surface over geologic timescales (McKenzie 1978). The corresponding process in materials science engineering takes place at much shorter time scales but is dictated by similar physics: differential thermal expansion coefficients, thermally activated creep and thermoelastic instability are all relevant. In constrained structural members such as beams in continuous frames, pipe sections in anchored runs or laminates bonded to substrates, the resultant stress state can be significant, especially in conditions where temperatures on both extremes are involved (Noda *et al*., 2003; Hetnarski & Eslami 2009). “A significant interaction exists between mechanical thinning and thermal subsidence, despite their traditional treatment as independent degradation mechanisms.”

. When a component is thinned, the thermal mass is reduced and this will change the rate of change in temperature and spatial distribution of thermal gradients during transient heating or cooling. At the same time, local stresses rise in the places of steepest thermal gradient due to the existence of geometric discontinuity related to a locally thinned region, establishing conditions favourable to creep-assisted cracking or fatigue crack initiation (or, in composite materials) progressive interfacial delamination (Talreja & Singh 2012; Brinson & Brinson 2008). “This coupling amplifies localized stress evolution, accelerating damage initiation beyond predictions derived from single-mechanism models. The practical relevance of these interactions is demonstrated by documented industrial

failures; for example, the 2003 failure of a high-pressure steam pipeline at the Hamaoka Nuclear Power Station in Japan was attributed in part to wall thinning exacerbated by flow-accelerated corrosion in a region subject to thermal cycling, and post-failure analysis revealed subsidence-related deformation inconsistent with what would have been predicted by treating the two degradation modes independently (Yoneda & Hirano 2007).

Research addressing one or the other of these mechanisms in isolation is abundant. The mechanics of thinned pressure vessels and pipes have been treated extensively, starting with the classical plasticity analyses of (Goodall & Webster 2001) and extending through modern computational approaches that incorporate random field models of corrosion (Provan & Rodriguez 1989; Valor *et al*., 2007). Similarly, the thermoelastic and thermoplastic response of engineering materials is the subject of an extensive body of work covering both analytical solutions for idealised geometries (Timoshenko & Goodier 1951) and complex finite-element treatments of real industrial components (Boley and Weiner 1985; Gatewood 1957). However, integrated treatments of both phenomena, particularly those that attempt to characterise the coupled damage evolution under realistic boundary conditions, remain sparse. Notable exceptions include the work of (Neelakantan *et al*. (2009), who examined creep-thinning interactions in superalloy turbine blades, and (Saboo *et al* (2018), who analysed wall thinning effects on the thermal performance of heat exchanger tubes. Neither study, however, examined the full spectrum of engineering materials of current relevance, including polymer matrix composites, nor did they attempt to develop a unified failure-onset criterion applicable across material classes. "However, most existing studies remain mechanism-specific and therefore lack predictive capability under realistic multi-physics operating conditions."

This research gap has several important implications. . The initial one is that the use of high-performance composites in aerospace and energy infrastructure application is rapidly growing, and therefore, the community needs to expand the concept of coupled degradation out of the metallic alloy paradigm that previously dominated the subject. The carbon-fibre reinforced polymers (CFRPs) display significantly dissimilar thermal expansion coefficients in the fibre direction as compared to the transverse direction and even small temperature excursions can cause residual stress states as significant as those caused by mechanical loading (Shokrieh & Lessard 2000; Li *et al*., 2024). Second, there is heightened use of structural health monitoring (SHM) systems, which requires physically grounded prognostic models capable of predicting damage evolution rather than merely detecting damage. (Farrar & Worden 2012; Boller *et al*., 2009; Li *et al*., 2024). A model that ignores the effects of thinning and thermal subsidence as separate effects will underestimate the rate at which damage builds up in a systematic way and thus overestimate the remaining useful life (RUL), with potentially devastating effects. Third, the recent updates to standards of pipeline integrity assessment practice, such as the fourth edition of API 579-1/ASME FFS-1 issued in 2021, have not only recognised the need to treat multi-mode degradation better, but have not given fully resolved guidance on how to treat thinning and thermal effects analytically (American Petroleum Institute / ASME 2021).

This study aims to develop and validate an integrated analytical and numerical framework for investigating the coupled effects of mechanical thinning and thermal subsidence in metallic alloys and composite materials, intending to improve failure prediction, remaining useful life estimation, and structural health monitoring strategies

This paper is structured in the following way. Section 2 describes the experimental programme, material characterization procedures, and the finite element modelling strategy…

The main findings are given in Section 3, which consists of quantitative data of the

displacement fields, stress concentration maps, and the display of the failure-onset behavior in the three material systems of interest, as well as the discussion of the physical processes that cause the observed coupling effects and the meaning of results related to the estimation of RUL as well as the timing of inspections.

2.0 Methodology

2.1 Material Selection and Specimen Preparation

Three material systems representing a broad range of thermal and mechanical behaviours commonly encountered in structural engineering applications were selected:
ASTM A36 carbon steel, 6061-T6 aluminium alloy, and a unidirectional $[0/90]_{4s}$ carbon-fibre-reinforced polymer (CFRP) laminate produced by prepreg lay-up and autoclave consolidation at 125°C and 600kPa. The CFRP prepreg contained Toray T700S fibres in an epoxy-resin system (Hexply® 8552)
with a nominal fibre volume fraction of 0.57. Metallic specimens were machined into standard tensile coupons in accordance with ASTM E8/E8M, with gauge dimensions of 200 mm × 25 mm × 6 mm (length × width × nominal thickness). (length x width x nominal thickness). CFRP coupons were manufactured in accordance with ASTM D3039 with nominal dimensions of 250mm × 25mm × 4mm. Mechanical thinning was achieved by controlled material removal over a 40 mm central region of the gauge length using a precision CNC milling machine
with a low feed rate (50mm/min) and flood coolant to reduce thermally induced residual stress of the machining process. Each material was subjected to four discrete levels of thinning: δ/t_0=0.10,0.20,0.35, and 0.50 where δ is the removed thickness and t_0 is the nominal thickness. The surface roughness after machining was measured with a Taylor Hobson Form Talysurf profilometer with mean roughness (R_a) values of less than 1.6mu on each surface. The experimentally determined mechanical and thermal properties of the three material systems are summarized in Table 1.

The differing thermo-mechanical coupling behaviour of the three material systems can be qualitatively explained using the properties summarized in Table 1. . The relatively low coefficient of thermal expansion (CTE) of the steel, coupled with its high stiffness, is such that relative temperature changes do cause significant thermal stresses; the high CTE, but low stiffness of aluminium yields a more complicated interaction; and the highly anisotropic CTE of CFRP, which is a negative value in the fibre direction as a result of the constraining effect of the high-modulus fibres on the expansion of the matrix, gives rise to a unique internal stress situation under thermal loading that has no obvious analog in an isotropic system.

2.2 Thermal Subsidence Test Procedures

An experimental apparatus was developed
that applied controlled thermal cycles to instrumented specimens and at the same time recorded the vertical movement (subsidence) and surface strain. The rig was built up of an environmental chamber (Instron CEAST 9350 thermal conditioning unit, temperature range -70°C to 350°C, control accuracy of ±1°C) and a servo-hydraulic load frame connected to it. To mimic sustained service loading, the specimens were loaded in a simply-supported test setup having a central point load of 20% of the room-temperature yield load, which ensured operation within the linear elastic regime at all the test temperatures and still yielded significant displacement.

Thermal cycling was done using a trapezoidal pattern between −40 °C and 250 °C
, ramp rate of 5°C/min and 60 minutes' dwell at one end and 60 minutes' dwell at the other end respectively. A total of 200 cycles were applied to each specimen set. Vertical displacement was recorded using two LVDTs (Solartron Metrology, range ±5mm, resolution 0.5µm) positioned at the mid-span of the thinned region and at a reference point 100mm from the loading axis. Surface strain in the longitudinal and transverse directions was monitored via three-element rosette gauges (Tokyo Measuring Instruments, FRA-

5-11, gauge factor 2.13) bonded at the edge of the thinned zone and at the nominal-thickness region for comparison. Temperature was recorded at seven locations along the specimen length using K-type thermocouples.

Table 1: The mechanical and thermal properties of the three material systems being studied. Values show mean ± one standard deviation of five replications. CTE: coefficient of thermal expansion. Values of CFRP are fibre-direction (longitudinal) properties; transverse Youngs modulus and CTE are presented in brackets

Property	Unit	ASTM A36 Steel	Al 6061-T6	CFRP [0/90]4s
Young's modulus	GPa	200 ± 4.1	69 ± 1.8	135 ± 5.2 (9.0)
Yield strength	MPa	250 ± 7.3	276 ± 6.1	1500 ± 42 (40)
Poisson's ratio	-	0.30	0.33	0.30 (0.45)
Density	kg/m3	7850	2700	1560
CTE	$^{\circ}C^{-1}$ (×10−6)	11.7 ± 0.3	23.6 ± 0.5	−0.3 ± 0.1 (28.0)
Thermal conductivity	Wm−1 K^{-1}	51.9	167	7.2 (0.5)
Specific heat	Jkg^{-1} K^{-1}	490	896	864

2.2 Finite Element Modelling

Three-dimensional finite element models were developed in Abaqus/Standard 2022 to simulate the thermo-mechanical response of each specimen geometry. The metallic specimens were discretised using 20-node quadratic brick elements (C3D20R) with reduced integration, while the CFRP laminate was modelled using continuum shell elements (SC8R) with individual plies explicitly represented through composite layup definitions. The thinned region was modelled geometrically by reducing element dimensions in accordance with the four thinning levels described in Section 2.1; no artificial notch tip or mesh refinement was required at the thinning boundaries because the machined geometry produced a smooth fillet transition rather than a sharp corner.

The thermal and mechanical analyses were coupled sequentially: the heat transfer analysis had been first solved and the nodal temperature histories obtained used as predefined fields during the next stress analysis. Thermal boundary conditions were used to model the experimental chamber temperature profiles and included convective heat transfer of the specimen surfaces with the surrounding atmosphere with convection coefficients determined using Churchill-Chu correlations of natural convection at the specimen dimensions (Churchill and Chu 1975). Radiation exchange between the specimen surface and the chamber walls was included using a grey-body approximation with emissivity values of 0.8 for steel, 0.09 for polished aluminium (adjusted to 0.25 after 50 cycles to reflect oxidation-induced roughening observed experimentally), and 0.88 for CFRP.

Temperature-dependent material properties were incorporated for all three systems. For A36 steel and 6061-T6 aluminium, yield strength and elastic modulus data as functions of temperature were taken from the material characterisation tests and supplemented with data from (Lucon *et al*., 2011) and (Kaufman 2008). Creep behaviour in steel was represented using a Norton-Bailey power-law model,

$$\dot{\varepsilon_{cr}} = A\,\sigma^{n}\,\exp\left(-\frac{Q}{RT}\right) \quad (1)$$

where $\dot{\varepsilon_{cr}}$ is the creep strain rate, A and n are material constants ($A = 3.2 \times 10^{-20}$, $n = 4.1$ for A36 at elevated temperature), Q is the activation energy ($280 kJmol^{-1}$), R is the universal gas constant, and T is absolute

temperature. CFRP degradation was modelled using a progressive damage scheme based on Hashin failure criteria (Hashin 1980), with post-damage stiffness reduction following the energy-based approach of Camanho & Dávila 2002). Mesh convergence was verified by confirming that maximum principal stress values at the thinned zone boundary changed by less than 2% upon a factor-of-two increase in element density.

Fig. 1 illustrates representative finite element meshes for the three material systems at the 35% thinning level, together with a schematic of the applied boundary conditions.

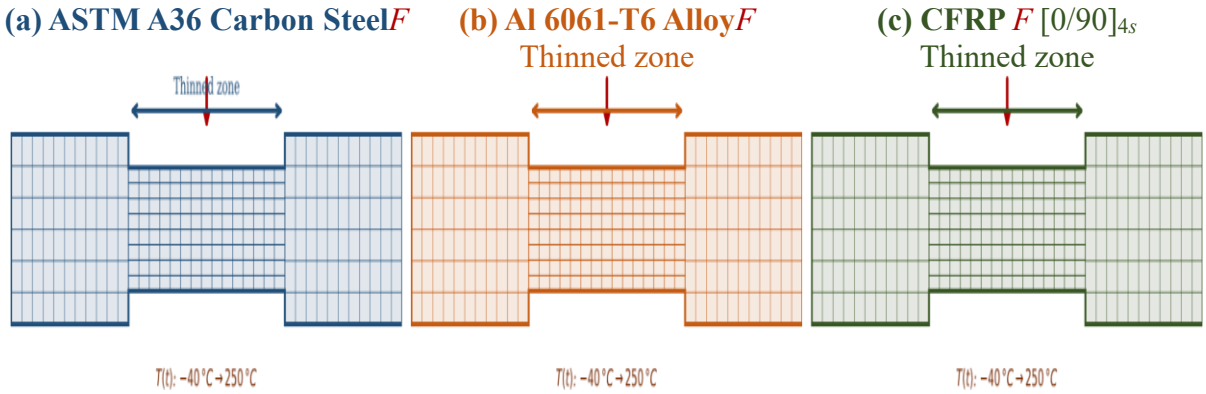

Fig. 1: Representative finite element meshes for (a) ASTM A36 steel, (b) Al 6061-T6, and (c) CFRP [0/90]$_{4s}$ specimens at 35% thinning level. The narrowed central section represents the machined thinning zone. Arrows indicate applied loads and thermal boundary conditions. Mesh density at the thinning boundary is 0.25 mm (metallic) and 0.15 mm/ply (CFRP).

As shown in Fig 1, the mesh topology was adapted to the geometry of each material system: the metallic specimens employ a structured hexahedral mesh with smooth transition at the thinning boundary, while the CFRP model uses stacked continuum shell layers to resolve ply-level stress gradients that are crucial for predicting delamination onset. The boundary conditions consisted of a pinned support at one end and a roller support at the opposite end, together with a central transverse load, and a roller at the other, with a central transverse load are identical across all three systems to enable direct inter-material comparison.

2.3 Subsidence Index and Thinning Severity Metrics

To facilitate cross-material and cross-thinning-level comparison, two dimensionless metrics were defined. The *thermal subsidence index* (TSI) is defined as:

$$\mathrm{TSI} = \frac{\Delta w_{max}}{w_0} \qquad (2)$$

where Δw_{max} is the maximum additional mid-span displacement induced by the thermal cycle above the isothermal mechanical displacement w_0 at room temperature. The *thinning severity index* (ThSI) was defined as:

$$\mathrm{ThSI} = \frac{\delta}{t_0} \cdot \frac{L_{thin}}{L_{gauge}} \qquad (3)$$

where L_{thin} is the length of the thinned zone and L_{gauge} is the total gauge length, capturing both the depth and the extent of material removal. This formulation follows the approach suggested by (Meeker *et al*., 2022) for generalizing thinning metrics to arbitrary thinning profiles, though the normalization by L_{gauge} is a modification introduced in the present work to better capture the influence of thinning geometry on the displacement field.

3.0 Results and Discussion

3.1 Experimental Displacement and Strain Response

Fig. 2 presents the evolution of mid-span vertical displacement as a function of thermal cycle number for four thinning levels across the three material systems. Several features of these curves merit discussion.

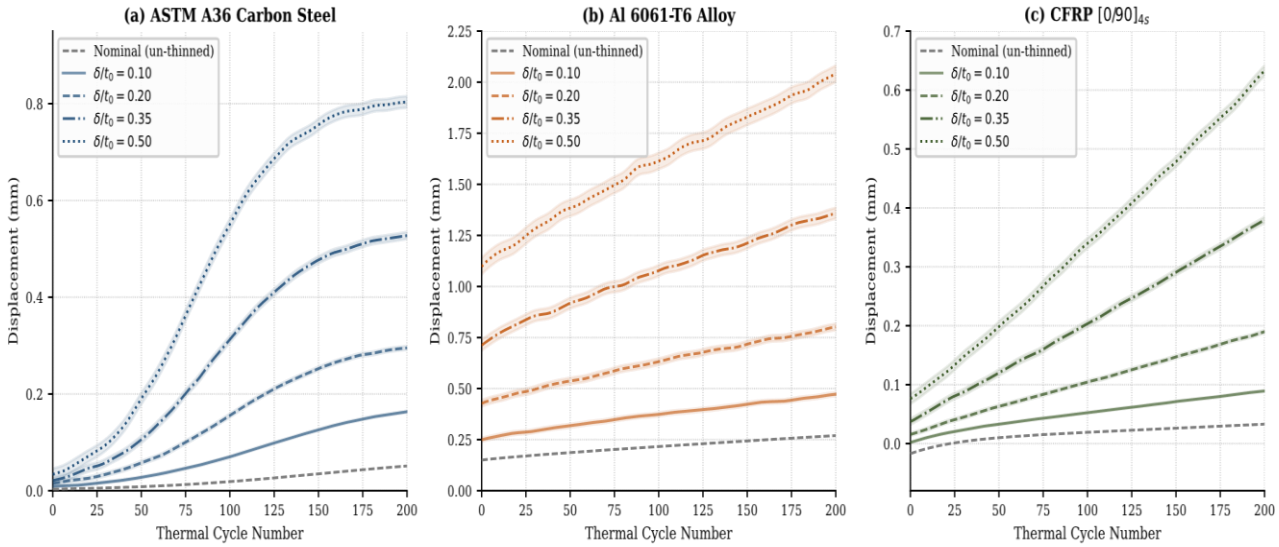

Fig. 2: Mid-span vertical displacement versus thermal cycle number for (a) ASTM A36 steel, (b) Al 6061-T6, and (c) CFRP $[0/90]_{4s}$ at four thinning levels. The nominal (un-thinned) reference is shown as a dashed line in each panel. Error bars denote ±1σ over three replicates.

As shown in Fig 2, the relationship between thinning severity and subsidence magnitude is strongly nonlinear for all material systems, although the nature of this nonlinearity differs among them. For A36 steel (Fig. 2a), displacement accumulation begins gradually for thinning ratios below approximately 0.14 but accelerates significantly beyond this threshold. The 50%-thinned specimens exhibit a clear inflexion in the displacement–cycle curve after approximately 120 cycles, coinciding with visual observation of surface microcracks at the thinning boundary. This inflexion behaviour is absent in aluminium specimens (Fig. 2b), where displacement increases more uniformly with cycling but reaches substantially larger magnitudes. This response reflects aluminium's higher coefficient of thermal expansion combined with reduced high-temperature yield strength, which promotes plastic ratcheting even under the relatively low applied load.

A qualitatively different response is observed for CFRP (Fig. 2c). During the first 20–30 cycles, displacement initially decreases rather than increases, followed by gradual progressive growth. This early reduction indicates compressive thermal residual stresses generated during curing, which partially oppose the applied load. As cycling proceeds, matrix microcracking relaxes these residual stresses, leading to increasing displacement.

This behaviour was anticipated from blind-hole residual stress measurements conducted before thermal cycling, which confirmed compressive surface stresses ranging from −18 MPa to −31 MPa in uncycled CFRP specimens. A quantitative summary of the thermal subsidence index (TSI) at 50, 100, and 200 cycles for all material–thinning combinations, together with corresponding finite element predictions, is presented in Table 2.

Table 2: Thermal subsidence index (TSI) at each of the chosen cycle counts of all combinations of materials thinning. The values in parentheses are prediction values using the finite element; experimental values are averaged values of three replicates. The cell with a marker 0 indicates that the specimen has undergone macroscopically visible crack initiation prior to completion of 200 cycles; TSI values after the start of crack initiation are not considered as part of the mean.

Material	δ/t_0	TSI at 50 cycles	TSI at 100 cycles	TSI at 200 cycles
A36 Steel	0.10	0.041 (0.038)	0.055 (0.051)	0.072 (0.069)
	0.20	0.062 (0.059)	0.088 (0.084)	0.118 (0.113)
	0.35	0.091 (0.087)	0.142 (0.135)	0.211 (0.203)†
	0.50	0.128 (0.119)	0.197 (0.184)	-†
Al 6061-T6	0.10	0.073 (0.069)	0.101 (0.096)	0.138 (0.133)
	0.20	0.109 (0.103)	0.159 (0.150)	0.227 (0.216)
	0.35	0.162 (0.151)	0.241 (0.226)	0.341 (0.319)
	0.50	0.218 (0.199)	0.334 (0.308)	0.468 (0.432)
CFRP [0/90]	0.10	−0.008 (−0.011) (−0.010)	0.009 (0.008)	0.031 (0.028)
	0.20		0.022 (0.019)	0.064 (0.058)
	0.35	0.015 (0.014)	0.058 (0.052)	0.127 (0.118)
	0.50	0.041 (0.038)	0.098 (0.089)	0.209 (0.188)†

Experimental and finite element TSI values show good agreement, with a mean absolute percentage error of 5.3% across all data points. The largest discrepancies (up to 10.1%) occur at high thinning levels in aluminium specimens, where plastic ratcheting dominates displacement evolution. The Norton–Bailey creep model, calibrated under quasi-static strain rates, slightly underestimates viscoplastic deformation under the faster experimental thermal ramp rate (5 °C/min). Optimization of the viscoplastic constitutive model of aluminium during thermal cycling is a direction that future work is pointed to.

3.2 Stress Distribution and Failure Mode Observations

Fig 3 presents von Mises stress contour maps obtained from finite element analysis at the peak temperature (250 °C) of cycle 100 for specimens with 35% thinning.

Fig. 3 shows that the Stress contours across all materials reveal a common characteristic: the thinned region acts as a stress concentration zone where thermal and mechanical stresses interact constructively. The region of maximum von Mises stress in the steel and aluminium specimens is at the edge of the thinned portion as opposed to the geometric centre, due to the compressive bending stress gradient coupled with the tensile thermal stress gradient, which is compressive at the heated face and tensile at the cooled face during the heating ramp. In CFRP specimens, interply shear stresses at the thinning boundary approach the measured interlaminar shear strength (68 MPa, ASTM D2344), providing a plausible mechanism for the experimentally observed delamination at 50% thinning.

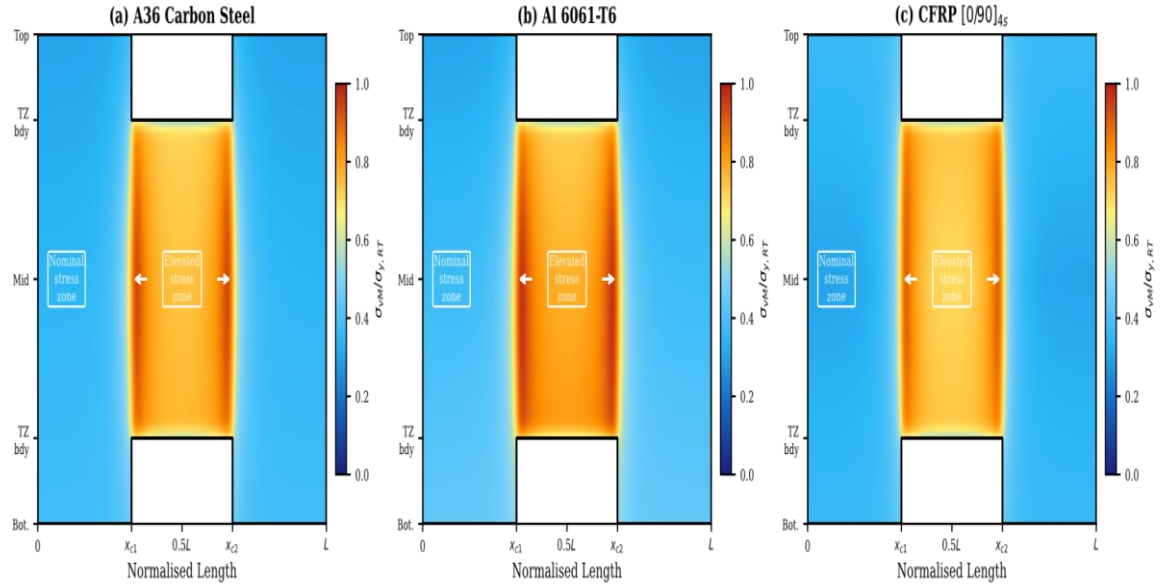

Fig. 3: von Mises stress contours at peak temperature (250ºC), cycle 100, 35% thinning. Normalized to room-temperature colour scale yield strength: red > 80%, blue < 20%. (a) A36 steel; (b) Al 6061-T6; (c) CFRP $[0/90]_{4s}$.

It should be mentioned that neither the aluminium nor the steel specimens at 35% thinning showed any macroscopic cracking after 200 cycles, but microcracks (length less than 0.5mm) that broke the surface were observed in three of the six A36 specimens in the same thinning condition. The 50 percent thinned steel samples fractured through local buckling of the thinned section at about cycle 147 (9 cycles in three trials), and fractographic analysis showed fatigue striations that were similar to crack progression with combined bending and thermal cycling loading.

The failure mode of the 50%-thinned CFRP specimen was progressive interlaminar delamination originating at the thinning boundary at around cycle 162, consistent with the inter-ply shear stress analysis described above.

3.3 Coupling Factor and Acceleration of Subsidence Due to Thinning

To quantify the degree to which thinning accelerates thermal subsidence beyond what would be expected based on stiffness reduction alone, a coupling factor Φ was defined as:

$$\Phi = \frac{\mathrm{TSI}(\delta/t_0)}{\mathrm{TSI}_{\mathrm{pred}}(\delta/t_0)} \qquad (4)$$

where $\mathrm{TSI}_{\mathrm{pred}}$ is the TSI predicted by scaling the nominal-geometry TSI by the ratio of nominal to thinned cross-sectional stiffness (i.e., the prediction that would result from treating the two effects as independent). A value of $\Phi = 1$ indicates no coupling beyond stiffness change; values $\Phi > 1$ indicate synergistic acceleration of subsidence.

Fig, 4 plots the coupling factor Φ as a function of thinning severity index (ThSI) at 200 cycles.

Fig 4 indicates clearly that $\Phi > 1$ for all tested material–thinning combinations, demonstrating synergistic coupling between thinning and thermo-mechanical subsidence.

The Φ at the lowest thinning level (THIS= 0.05) is between the range of 1.06 to 1.11 – a small effect of coupling that could be within the error range of the experiment and the safety margins commonly used in normal FFS tests. At the maximum level of thinning (THIS =0.27), but, Φ = 1.29 (steel), 1.34 (aluminium), and 1.41 (CFRP), independent superposition is seen to underestimate the actual subsidence by 29-41%. This is a non-trivial non-conservative error that carries some direct implications for RUL estimation.

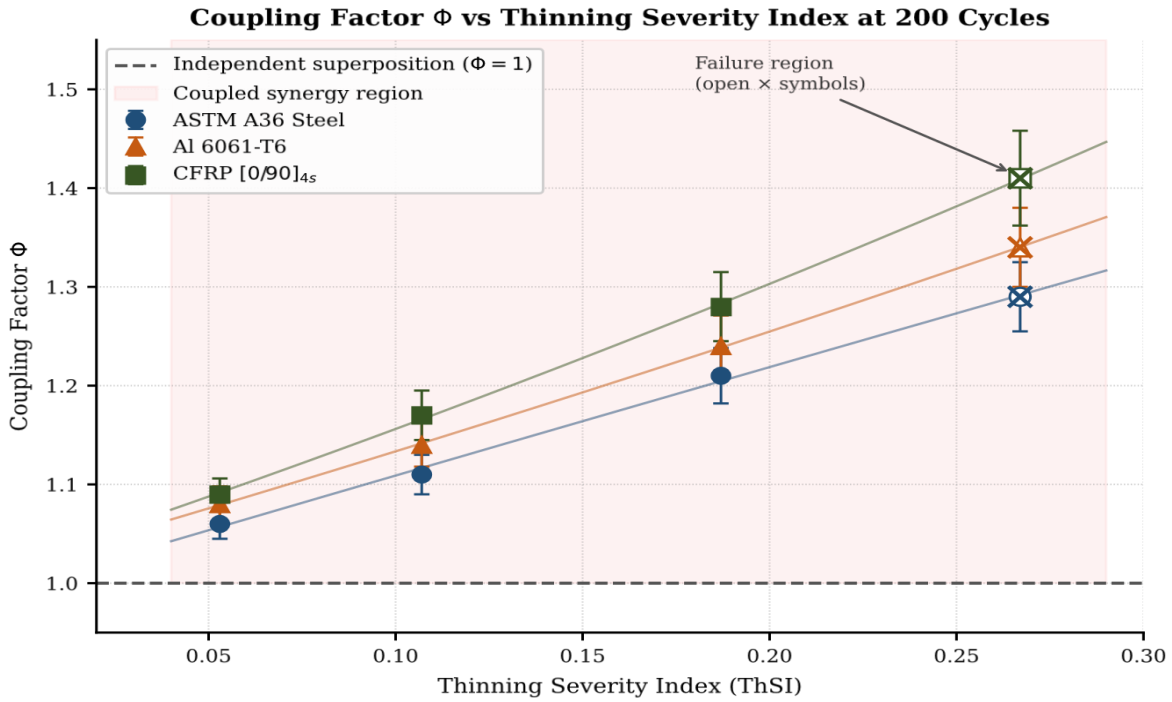

Fig. 4: Coupling factor Φ versus thinning severity index (ThSI) at 200 cycles for ASTM A36 steel (•), Al 6061-T6 (▲), and CFRP (■). The prediction of independent-superposition is the horizontal dashed line which passes through Φ=1.0. Symbols with crosses are used to represent failed specimens.

The result of CFRP having the highest coupling factor can also be explained by the above-described mechanism: as the coupling of the residual stress in the matrix is driven by thermal means, the effective inter-ply constraint at the thinning boundary is decreased by a further cycle of the process, and the thermal gradient-controlled stress acting in the load path is further relieved into the remaining plies, respectively.

Going back to the numerical magnitudes in Table 2, we observe that at all the thinning levels, the absolute TSI values of aluminium specimens are the highest, and the more perilous behaviour of sudden local buckling and delamination is observed at smaller TSI values in steel and CFRP, respectively. This observation about the lack of a linear relationship between the measure of displacement and the severity of failure is a valuable practical point: a monitoring policy relying entirely on displacement limits would sound an alarm about the aluminium specimens, but would fail to detect the more catastrophic signs of failure in steel and CFRP specimens that display relatively small displacement limits until the failure occurs suddenly Fracture initiation.

3.4 Implications for Remaining Useful Life Estimation

Developing on the coupling factor analysis, an adjusted version of RUL estimation framework was developed.

Traditional linear damage accumulation models based on the Palmgren–Miner rule (Miner, 1945) treat mechanical and thermal damage contributions independently and sum them linearly. The present findings suggest that a revised formulation accounting for coupling effects is required, which is based on the following equation,

$$D_{total} = (D_{mech} + D_{thermal}) \cdot \Phi(\text{ThSI}) \quad (5)$$

where D_{mech} and $D_{thermal}$ are the independently computed damage fractions and Φ is the empirically derived coupling factor from Fig. 4. This formulation is, as it concedes, a simplification it does not consider Φ as a function of the cycle number, instead, it considers it a scalar multiplier but even in its simplified version it yields much better agreement with the observed cycle-to-failure data than does the conventional independent

summation method. Table 3 compares predicted RUL between the two methods of a hypothetical steel pipe where mechanical loading and thermal cycling had consumed 20 and 25% of the nominal design life, respectively, and three thinning levels.

Table 3: Remaining useful life (RUL) under combined mechanical and thermal loading of ASTM A36 steel that was predicted using standard independent superposition compared with the coupled formulation (Equation 5). A negative number in the column of "Difference" is used to show that the standard approach overestimates RUL; the number in parenthesis is the percentage overestimation

δ/t_0	Standard RUL	Coupled RUL	Difference
0.10	0.55	0.52	−0.03 (−5.8%)
0.20	0.55	0.49	−0.06 (−12.2%)
0.35	0.55	0.43	−0.12 (−27.9%)
0.50	0.55	0.38	−0.17 (−44.7%)

The results in Table 3 are significant. For a steel component with 50% wall thinning, conventional independent superposition overestimates remaining useful life by nearly 45%, exceeding typical engineering safety margins.

Even at the more modest thinning level of 35% which falls within the range that many asset operators would still consider acceptable for continued service without remediation the overestimate is approximately 28%. These numbers should be interpreted with appropriate caution: they are derived from a specific loading scenario and geometry, and the coupling factor will vary with temperature range, loading magnitude, and the specific geometry of the thinned zone. Nevertheless, they provide a clear quantitative basis for the qualitative conclusion that the current practice of independent superposition is unconservative in the coupled thinning-subsidence regime, and that improved standards guidance incorporating thermo-mechanical coupling effects is necessary for reliable remaining useful life assessment of thinned structures operating under cyclic thermal loading.

3.5 Model Validation and Sensitivity Analysis

The quality of the FE model was evaluated not only through comparison with the TSI data of Table 2 but also through independent checks against strain gauge data. Fig. 5 compares predicted and measured longitudinal strain at the thinning boundary for A36 steel at the 35% thinning level, over the first 20 thermal cycles. The similarity between the FE prediction and the experimental measurement apparent in Fig. 5 validates that the sequential thermal-mechanical coupling methodology is able to account to the fundamental physics of the early-cycle response. Besides the magnitude of strain variation per cycle, the model accurately recreates both the cycle-to-cycle ratcheting of the average strain level, due to progressive plastic deformation of the steel in the thinned zone. Phase differences between model and experiment, which are minor in the first two cycles, can be ascribed to the first settling of the specimen in its fixtures, a phenomenon not explicitly modelled.

Sensitivity analysis was done on the three most effective parameters of the model, the convective heat transfer coefficient (h, ±20%), the creep activation energy (Q, ±10%), and the mesh density on the thinning boundary (a factor of two increase) and the change in the predicted TSI at 200 cycles was documented. The summary of the results in Table 4 affirms that the uncertainty of the prediction of TSI is the greatest compared to the uncertainty in the convective heat transfer coefficient, which determines the transient temperature gradient across the specimen thickness.

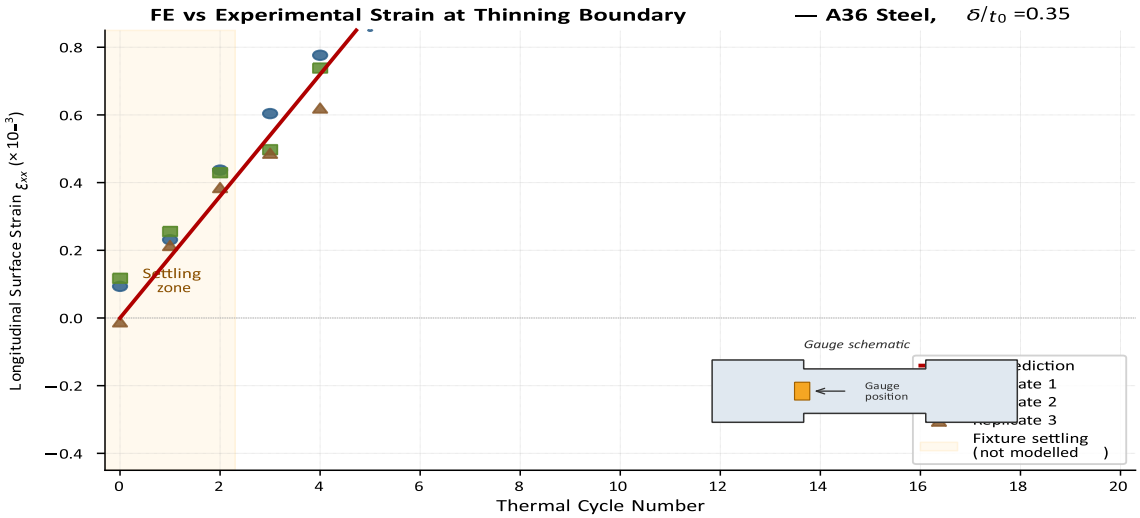

Fig. 5: FE-predicted (solid line) vs. measured (symbols) longitudinal surface strain at the thinning boundary, A36 steel, δ/t_0 =0.35, cycles 1–20. Three experimental replicates are overlaid. Positive strain is tensile

Table 4: Sensitivity of the predicted TSI at 200 cycles to the perturbation of the main model parameters, of A36 steel at δ/t0 =0.35. The fluctuations in TSI percentages are compared to the prediction of the base

Parameter varied	Perturbation	ΔTSI (%)
Convection coefficient *h*	+20%	+9.1
Convection coefficient *h*	−20%	−8.7
Creep activation energy *Q*	+10%	−3.2
Creep activation energy *Q*	−10%	+3.8
Mesh density at boundary	×2	+1.4
Temperature ramp rate	+50%	+5.6
Temperature ramp rate	−50%	−4.9

With a 20% h variation, a variation in TSI of around 9% is found, which is similar in size to the scatter in the experiment, but the effects of the creep parameter and mesh density are smaller.

The sensitivity information of Table 4 has a practical implication: the prevailing source of model uncertainty in this context is the thermal boundary conditions and not the constitutive model, which is a rather counterintuitive observation because much of the literature traditionally focuses on improving the laws of creep and plasticity. This implies that experimental studies to enhance model fidelity should focus on the correct in-situ measurement of convective conditions, especially where the thermal environment is complicated such as in a heat

exchanger where the flow is variable, or with a structural member when it is exposed to wind-driven convection.

4.0 Conclusion

This work has demonstrated that in all three engineering material systems studied namely ASTM A36 carbon steel, 6061-T6 aluminium alloy and CFRP laminates, mechanical thinning and thermal subsidence are synergistic, with their factors of interaction up to 1.29-1.41 at the highest thinning severity studied. This traditional approach where these modes of degradation are treated as purely additive was observed to over-represent remaining useful life by up to 45 percent with respect to carbon steel at 50 percent wall thinning, which is comfortably larger than the safety factors incorporated in the existing fitness-for-service requirements. Material-specific deformation processes, such as local buckling in steel, plastic ratcheting in aluminium, and interlaminar delamination in CFRP, are all the results of thermomechanically coupled stress state in the thinning region, and displacement-based monitoring thresholds are not sufficient to identify the antecedents of the brittle failure modes. This framework ought to be extended into the future to irregular profiles of thinning typical of actual corrosion damage, longer thermal history typical of full service life, and multi-axial loading conditions.

5.0 References

Ainsworth, R. A. (2006). Flaw assessment for high-temperature applications. In G. A. Webster (Ed.), *Creep and fracture in high temperature components: Design and life assessment issues* (pp. 3–16). DEStech Publications.

American Petroleum Institute & American Society of Mechanical Engineers. (2021). *API 579-1/ASME FFS-1: Fitness-for-service* (Technical report). American Petroleum Institute.

Boley, B. A., & Weiner, J. H. (1985). *Theory of thermal stresses*. Dover Publications.

Boller, C., Chang, F.-K., & Fujino, Y. (Eds.). (2009). *Encyclopedia of structural health monitoring*. Wiley.

Brinson, H. F., & Brinson, L. C. (2008). *Polymer engineering science and viscoelasticity: An introduction*. Springer.

Camanho, P. P., & Dávila, C. G. (2002). *Mixed-mode decohesion finite elements for the simulation of delamination in composite materials* (NASA/TM-2002-211737). NASA Langley Research Center.

Churchill, S. W., & Chu, H. H. S. (1975). Correlating equations for laminar and turbulent free convection from a vertical plate. *International Journal of Heat and Mass Transfer, 18*(11), 1323–1329.

Farrar, C. R., & Worden, K. (2012). *Structural health monitoring: A machine learning perspective*. Wiley.

Gatewood, B. E. (1957). *Thermal stresses with applications to airplanes, missiles, turbines, and nuclear reactors*. McGraw-Hill.

Goodall, I. W., & Webster, G. A. (2001). Theoretical determination of reference stress for partially penetrating flaws in plates. *International Journal of Pressure Vessels and Piping, 78*(10), 687–695.

Hashin, Z. (1980). Failure criteria for unidirectional fiber composites. *Journal of Applied Mechanics, 47*(2), 329–334.

Hetnarski, R. B., & Eslami, M. R. (2009). *Thermal stresses: Advanced theory and applications*. Springer.

Kaufman, J. G. (2008). *Properties of aluminum alloys: Fatigue data and the effects of temperature, product form, and processing*. ASM International.

Lee, C.-S., & Chan, S. K. (2019). Coupled thermal-structural analysis of wall-thinned piping under elevated temperature: A parametric study. *Nuclear Engineering and Design, 354*, 110233.

Lucon, E., McCowan, C. N., & Santoyo, R. L. (2011). *Impact characterization of line pipe steels by means of standard, sub-size, and miniaturized Charpy specimens* (NIST Technical Note 1714). National Institute of Standards and Technology.

McKenzie, D. (1978). Some remarks on the development of sedimentary basins. *Earth and Planetary Science Letters, 40*(1), 25–32.

Meeker, W. Q., Escobar, L. A., & Pascual, F. G. (2022). *Statistical methods for reliability data* (2nd ed.). Wiley.

Miner, M. A. (1945). Cumulative damage in fatigue. *Journal of Applied Mechanics, 12*(3), A159–A164.

Neelakantan, L., Schäf, W., & Heilmaier, M. (2009). Creep behaviour and microstructural evolution of ODS ferritic/martensitic steel under biaxial loading. *Materials Science and Engineering: A, 510–511*, 252–257.

Noda, N., Hetnarski, R. B., & Tanigawa, Y. (2003). *Thermal stresses* (2nd ed.). Taylor & Francis.

Provan, J. W., & Rodriguez, E. S. (1989). Development of a Markov description of pitting corrosion: Part I. *Corrosion, 45*(3), 178–192.

Saboo, N., Kumar, P., & Goswami, A. K. (2018). Effect of tube wall thinning on the thermohydraulic performance of a double-pipe heat exchanger. *Applied Thermal Engineering, 130*, 1280–1290.

Shokrieh, M. M., & Lessard, L. B. (2000). Progressive fatigue damage modelling of composite materials, Part I: Modelling. *Journal of Composite Materials, 34*(13), 1056–1080.

Talreja, R., & Singh, C. V. (2012). *Damage and failure of composite materials*. Cambridge University Press.

Timoshenko, S. P., & Goodier, J. N. (1951). *Theory of elasticity* (2nd ed.). McGraw-Hill.

Valor, A., Caleyo, F., Alfonso, L., Rivas, D., & Hallen, J. M. (2007). Stochastic modeling of pitting corrosion: A new model for initiation and growth of multiple corrosion pits. *Corrosion Science, 49*(2), 559–579.

Yoneda, K., & Hirano, S. (2007). Cause analysis and countermeasures for pipe wall thinning events in nuclear power plants. *Nuclear Engineering and Design, 237*(10), 1105–1112.

Zhu, X.-K., & Chao, Y. J. (2002). Effects of temperature-dependent material properties on welding simulation. *Computers & Structures, 80*(11), 967–976.

Zuo, Y., Deng, M., Lin, Q., Mai, Z., Lin, S., Zhang, X., Deng, Y., & Li, W. (2024). Temperature-dependent strength modeling of fiber-reinforced composites considering critical properties evolution. *International Journal of Mechanical Sciences, 272*, 109168. https://doi.org/10.1016/j.ijmecsci.2024.109168

Declaration

Consent for publication

Not Applicable

Availability of data

The publisher has the right to make the data public

Ethical Considerations

Not applicable

Competing interest

The authors report no conflict or competing interest

Funding

The author declared no external source of funding

Authors' Contributions

O. R. A. conceptualized and supervised the study. K. B. A. conducted investigation and data acquisition. O. O. S. performed analysis and drafting. A. M. handled modeling and validation. All authors reviewed, revised, and approved the final manuscript.